Journal of Photonics for Energy

PhotonicsforEnergy.SPIEDigitalLibrary.org

Enhanced efficiency of Schottky-barrier solar cell with periodically nonhomogeneous indium gallium nitride layer

Tom H. Anderson
Tom G. Mackay
Akhlesh Lakhtakia

SPIE.

Tom H. Anderson, Tom G. Mackay, Akhlesh Lakhtakia, "Enhanced efficiency of Schottky-barrier solar cell with periodically nonhomogeneous indium gallium nitride layer," *J. Photon. Energy* **7**(1), 014502 (2017), doi: 10.1117/1.JPE.7.014502.

Enhanced efficiency of Schottky-barrier solar cell with periodically nonhomogeneous indium gallium nitride layer

Tom H. Anderson,[a,b] Tom G. Mackay,[a,b,*] and Akhlesh Lakhtakia[b]

[a]University of Edinburgh, School of Mathematics and Maxwell Institute for Mathematical Sciences, Edinburgh, Scotland, United Kingdom

[b]Pennsylvania State University, Department of Engineering Science and Mechanics, NanoMM—Nanoengineered Metamaterials Group, University Park, Pennsylvania, United States

Abstract. A two-dimensional finite-element model was developed to simulate the optoelectronic performance of a Schottky-barrier solar cell. The heart of this solar cell is a junction between a metal and a layer of *n*-doped indium gallium nitride ($In_\xi Ga_{1-\xi}N$) alloy sandwiched between a reflection-reducing front window and a periodically corrugated metallic back reflector. The bandgap of the $In_\xi Ga_{1-\xi}N$ layer was varied periodically in the thickness direction by varying the parameter $\xi \in (0,1)$. First, the frequency-domain Maxwell postulates were solved to determine the spatial profile of photon absorption and, thus, the generation of electron–hole pairs. The AM1.5G solar spectrum was taken to represent the incident solar flux. Next, the drift-diffusion equations were solved for the steady-state electron and hole densities. Numerical results indicate that a corrugated back reflector of a period of 600 nm is optimal for photon absorption when the $In_\xi Ga_{1-\xi}N$ layer is homogeneous. The efficiency of a solar cell with a periodically nonhomogeneous $In_\xi Ga_{1-\xi}N$ layer may be higher by as much as 26.8% compared to the analogous solar cell with a homogeneous $In_\xi Ga_{1-\xi}N$ layer. [DOI: 10.1117/1.JPE.7.014502]

Keywords: thin-film solar cell; Schottky junction; indium gallium nitride (InGaN); periodic back reflector; optical model; electronic model; nonhomogeneous composition.

Paper 16132 received Dec. 8, 2016; accepted for publication Jan. 18, 2017; published online Feb. 3, 2017.

1 Introduction

A variety of light-trapping strategies capitalizing on structures engineered on the order of the wavelength of solar light have been examined both experimentally and theoretically to enhance the efficiencies of solar cells.[1] These strategies include texturing the front surface of the solar cell,[2,3] incorporating a periodically corrugated metallic back reflector,[4–6] coating the front surface with an "antireflection" (AR) layer,[7,8] embedding nanoparticles inside the light-absorbing layer (s),[9–11] and using light concentrators.[12–15]

An attractive approach for boosting the solar-cell efficiency requires the use of photon-absorbing component materials whose electromagnetic properties are periodically nonhomogeneous along the thickness direction. Recently, it was demonstrated that the incorporation of a periodically nonhomogeneous intrinsic layer (i.e., *i* layer), along with a periodically corrugated back reflector, in amorphous silicon *p-i-n* junction solar cells can improve overall efficiency by up to 17%.[16] This improvement is likely due to

*Address all correspondence to: Tom G. Mackay, E-mail: T.Mackay@ed.ac.uk

i. the periodic corrugation of the metallic back reflector[4–6,17] facilitating the excitation of surface-plasmon-polariton waves[18–20] and waveguide modes[21] to intensify the electric field inside the semiconductor region, leading to an increase in the electron–hole pair (EHP) generation rate;
ii. the periodic nonhomogeneity of the *i*-layer that may facilitate the excitation of multiple surface-plasmon-polariton waves[22] and waveguide modes,[17] thereby further boosting the EHP generation rate; and
iii. the accompanying spatial gradient in the bandgap that may also aid charge separation and reduce the EHP recombination rate.[23,24]

The study described herein concerns an especially simple type of solar cell that has received scant attention from researchers to date: a Schottky-barrier solar cell.[25] The Schottky barrier is provided by a metal–semiconductor junction.[26,27] Recent theoretical studies,[28,29] along with an earlier experimental study,[30] have suggested that Schottky-barrier solar cells may be a particularly promising proposition if the semiconductor layer (i.e., the absorbing layer) was made from alloys of indium gallium nitride ($In_\xi Ga_{1-\xi}N$), since the bandgap for these alloys can closely match the range of energies of photons across the entire solar spectrum (i.e., 0.70 to 3.42 eV) by varying the relative proportions of indium and gallium through the parameter $\xi \in (0,1)$.[31] Specifically, indium nitride (i.e., $\xi = 1$) has a bandgap of 0.7 eV[32,33] and absorbs efficiently across the infrared regime in the solar spectrum, while gallium nitride (i.e., $\xi = 0$) has a bandgap of 3.42 eV and absorbs efficiently across the near-ultraviolet portion of the solar spectrum.

With current technologies, there are significant challenges to overcome in the production of $In_\xi Ga_{1-\xi}N$ alloys for all values of ξ, particularly for smaller-bandgap alloys. When the proportion of indium is large (i.e., $\xi \gtrsim 0.3$), poor crystal growth plagues the realization of solar-cell applications. Such poor growth results in decreased carrier transport, background *n* doping due to Fermi pinning above the conduction band edge,[34] and a bandgap that is greater than expected.[35,36] By using a Schottky-barrier junction with *n*-doped $In_\xi Ga_{1-\xi}N$, as opposed to a *p-i-n* junction, the difficulty of *p* doping the material is avoided.

In the following sections, a two-dimensional (2-D) numerical simulation is described for a Schottky-barrier solar cell made with $In_\xi Ga_{1-\xi}N$. It is essential that the coupled processes of optical absorption and electrical-current generation are simultaneously accommodated in the simulation. This is because a focus on the computation of only the optical (i.e., at full quantum efficiency) short-circuit current density, but not of the open-circuit voltage, overplays the importance of the EHP generation rate by not taking the EHP recombination rate into account.[16] In our simulation, particular attention is paid to the role of periodic nonhomogeneity of the absorbing material. Thus, the effect of periodically varying the fractional composition parameter ξ of $In_\xi Ga_{1-\xi}N$ in the direction perpendicular to the mean plane of the back reflector is explored, the back reflector being periodically corrugated in one direction. The model is briefly described in Secs. 2.1 and 2.2, with further details being available elsewhere.[16,37] Numerical results are presented in Secs. 3.1 and 3.2. Closing remarks are presented in Sec. 4.

2 Summary of the Model

2.1 *Physical Model*

A schematic diagram of the simulated Schottky-barrier solar cell is shown in Fig. 1. The back reflector is corrugated along the *x*-axis, and the *z* axis is normal to the plane of the Schottky contact and the mean plane of the back reflector. In the remainder of this paper, the term "width" refers to extent in the *x*-direction, while "thickness" refers to extent in the *z*-direction. Insolation is provided via an excitation port at $z = -L_{\text{Air}} - L_w - L_c$. A planar AR window made of an insulating material occupies the region $-L_w - L_c < z < -L_c$. To align with our earlier work, the optical permittivity of this layer was taken to be identical to that of aluminum-doped zinc oxide.[38]

The region $0 < z < L_z$ is occupied by *n*-doped $In_\xi Ga_{1-\xi}N$, forming a Schottky junction and two ohmic junctions with a metal in the region $0 < z < -L_c$. For calculations, the metal is assumed to be silver.[39] The Schottky contact of width L_s is centered at $x = 0$. The two

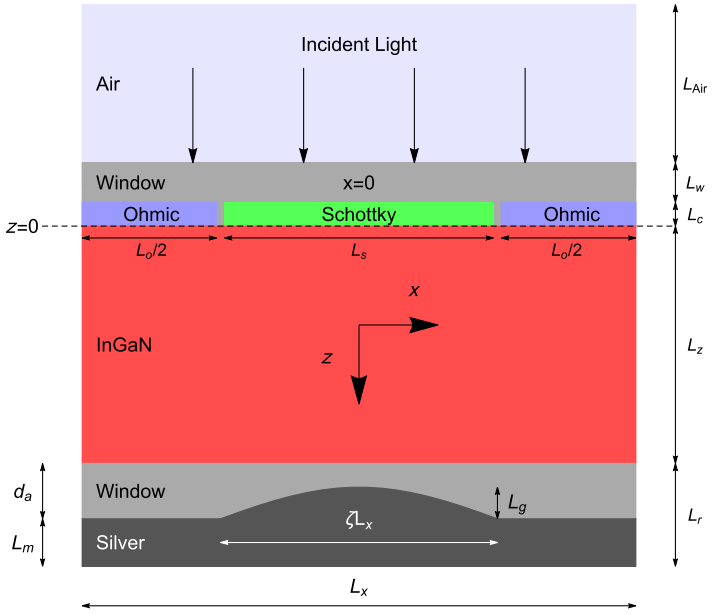

Fig. 1 Schematic illustration of a Schottky-barrier solar cell. Only one back-reflector period is shown [i.e., $-(L_x/2) < x < (L_x/2)$].

ohmic contacts, each of width $L_o/2$, are centered about $x = \pm(L_x - L_o/2)/2$. Note that $L_o + L_s < L_x$. The two regions between the metal contacts for $0 < z < L_c$ are occupied with the same material as the AR window that occupies $-L_w - L_c < z < -L_c$.

A silver back reflector, covered with an insulating window (made of the same material as the window that occupies $-L_w - L_c < z < -L_c$), occupies the region $L_z < z < L_z + L_r$. This back reflector is periodically corrugated in the x-direction with period L_x. The region $L_z < z < g(x)$ is filled with the window material, while the region $g(x) < z < L_z + L_r$ is filled with silver. The corrugation in the unit cell is specified by the function

$$g(x) = \begin{cases} L_z + d_a - L_g \cos\left(\frac{\pi x}{\zeta L_x}\right), & 2x/L_x \in (-\zeta, \zeta) \\ L_z + d_a, & 2x/L_x \notin (-\zeta, \zeta) \end{cases}, \tag{1}$$

where L_x is the corrugation period, $L_g \leq d_a$ is the corrugation height, and $\zeta \in (0,1]$ is the duty cycle. As the corrugation is invariant along the y-axis, our model is 2-D.

Absorption of the normally incident solar flux with AM1.5G spectrum[40] is calculated by solving the frequency-domain Maxwell postulates. The semiconductor charge-carrier drift-diffusion equations model the electron and hole density spatial distributions.[41,42] Because of the nonhomogeneity of the semiconductor (i.e., $In_\xi Ga_{1-\xi}N$), the effective dc electric field acting on (a) electrons includes a contribution from gradients in the electron affinity and (b) holes includes contributions from gradients in both the electron affinity and the bandgap. Direct, mid-gap Shockley–Read–Hall, and Auger recombination are all included in our simulation. The current density J, which is averaged over the Schottky contact (or, identically, both of the ohmic contacts), is calculated for a range of external biasing voltages V_{ext}.

By varying the proportion of indium relative to that of gallium, the bandgap of $In_\xi Ga_{1-\xi}N$ can be engineered to take any value from $E_g^{InN} = 0.7$ eV (i.e., for InN when $\xi = 1$) continuously through to $E_g^{GaN} = 3.42$ eV (i.e., for GaN when $\xi = 0$). Thus, allowing for nonhomogeneity in the z-direction, the $In_\xi Ga_{1-\xi}N$ alloy has bandgap given by

$$E_{g0}(z) = \xi(z) E_g^{InN} + [1 - \xi(z)] E_g^{GaN} - b\xi(z)[1 - \xi(z)], \qquad z \in (0, L_z), \tag{2}$$

where the bowing parameter $b = 1.43$ eV.[43] To estimate ξ for a material with a specific bandgap E_{g0}, Eq. (2) may be solved as

$$\xi(z) = \frac{b + (E_g^{\mathrm{GaN}} - E_g^{\mathrm{InN}}) - \sqrt{4b[E_{g0}(z) - E_g^{\mathrm{GaN}}] + (b + E_g^{\mathrm{GaN}} - E_g^{\mathrm{InN}})^2}}{2b}. \tag{3}$$

The electron affinity χ_0 for $\mathrm{In}_\xi\mathrm{Ga}_{1-\xi}\mathrm{N}$ is modeled in an analogous manner to the bandgap. Hence

$$\chi_0(z) = \xi(z)\chi^{\mathrm{InN}} + [1 - \xi(z)]\chi^{\mathrm{GaN}} - b\xi(z)[1 - \xi(z)], \qquad z \in (0, L_z), \tag{4}$$

where χ^{InN} and χ^{GaN} are the electron affinities of InN and GaN, respectively. For all other material parameters of $\mathrm{In}_\xi\mathrm{Ga}_{1-\xi}\mathrm{N}$, as described in the first column of Table 1, Vegard's law of linear interpolation[44] is assumed to apply, i.e.,

$$\tau^{\mathrm{In}_\xi\mathrm{Ga}_{1-\xi}\mathrm{N}}(z) = \xi(z)\tau^{\mathrm{InN}} + [1 - \xi(z)]\tau^{\mathrm{GaN}}, \qquad z \in (0, L_z), \tag{5}$$

where $\tau \in \{N_C, N_V, C_n, C_p, C_{\mathrm{rad}}, \alpha_{oc}\}$. Data for τ^{InN} and τ^{GaN} are provided in Table 1.

The narrowing of the bandgap associated with doping was incorporated through the Slotboom model.[45] While this model was developed for silicon, similar narrowing behavior under heavy-doping conditions has been observed in GaN.[46] When doped, the bandgap of the semiconductor narrows to $E_g = E_{g0} - \Delta E_g$, while the electron affinity reduces to

Table 1 Electronic data used for GaN and InN. The composition of $\mathrm{In}_\xi\mathrm{Ga}_{1-\xi}\mathrm{N}$ was estimated using Eq. (3), with linear interpolation used to estimate data for the semiconductor-filled region $0 < z < L_z$ with bandgaps not presented here in all cases, except for the electron affinity χ_0 which uses Eq. (4).

	Symbol	Unit	GaN	InN
Bandgap	E_g^*	eV	3.42	0.7
Electron affinity	χ_0	eV	4.1	5.6
Density of states (conduction band)	N_C	cm^{-3}	2.3×10^{18}	9.1×10^{17}
Density of states (valence band)	N_V	cm^{-3}	4.6×10^{19}	5.3×10^{19}
Electron mobility 1	$\mu_n^{(1)}$	$\mathrm{cm}^2\,\mathrm{V}^{-1}\,\mathrm{s}^{-1}$	295	1030
Electron mobility 2	$\mu_n^{(2)}$	$\mathrm{cm}^2\,\mathrm{V}^{-1}\,\mathrm{s}^{-1}$	1460	14150
Caughey–Thomas doping power (electrons)	δ_n	—	0.71	0.6959
Caughey–Thomas critical doping density (electrons)	$N_{\mathrm{n}}^{\mathrm{crit}}$	cm^{-3}	7.7×10^{16}	2.07×10^{16}
Hole mobility 1	$\mu_p^{(1)}$	$\mathrm{cm}^2\,\mathrm{V}^{-1}\,\mathrm{s}^{-1}$	3	3
Hole mobility 2	$\mu_p^{(2)}$	$\mathrm{cm}^2\,\mathrm{V}^{-1}\,\mathrm{s}^{-1}$	170	340
Caughey–Thomas doping power (holes)	δ_p	—	2	2
Caughey–Thomas critical doping density (holes)	$N_{\mathrm{p}}^{\mathrm{crit}}$	cm^{-3}	1×10^{18}	8×10^{17}
Auger recombination factor (electrons)	C_n	$\mathrm{cm}^6\,\mathrm{s}^{-1}$	1.5×10^{-30}	1.5×10^{-30}
Auger recombination factor (holes)	C_p	$\mathrm{cm}^6\,\mathrm{s}^{-1}$	1.5×10^{-30}	1.5×10^{-30}
Direct recombination factor	C_{rad}	$\mathrm{cm}^3\,\mathrm{s}^{-1}$	1.1×10^{-8}	2×10^{-10}
Slotboom reference energy	E_{ref}	eV	9×10^{-3}	9×10^{-3}
Slotboom reference concentration	N_{ref}	cm^{-3}	1×10^{17}	1×10^{17}
Conduction-band fraction	α_{oc}	—	0.9	0.9
Adachi refractive-index parameter A_A	A_A	—	9.31	13.55
Adachi refractive-index parameter B_A	B_A	—	3.03	2.05

$\chi = \chi_0 - \alpha_{oc}\Delta E_g$, with the conduction-band fraction α_{oc} being a material-specific parameter. Here, the bandgap narrowing is estimated as

$$\Delta E_g = E_{\text{ref}}\left\{\ln\left(\frac{N_d + N_a}{N_{\text{ref}}}\right) + \sqrt{\left[\ln\left(\frac{N_d + N_a}{N_{\text{ref}}}\right)\right]^2 + \frac{1}{2}}\right\}, \tag{6}$$

where N_d and N_a are the doping densities of the donor and the acceptor, respectively, and N_{ref} and E_{ref} are the empirically determined reference doping density and reference energy, respectively.

The real part of the optical refractive index of $\text{In}_\xi\text{Ga}_{1-\xi}\text{N}$ is

$$\text{Re}\{n\} = \text{Re}\left(\sqrt{A_A(\xi)\left\{\left[\frac{E_g(\xi)}{E_\gamma}\right]^2\left[2 - \sqrt{1 + \frac{E_\gamma}{E_g(\xi)}} - \sqrt{1 - \frac{E_\gamma}{E_g(\xi)}}\right] + B_A(\xi)\right\}}\right), \tag{7}$$

per the Adachi model,[29] where A_A and B_A are parameters given in Table 1. The photon energy is $E_\gamma = hc_0/\lambda_0$, where $h = 6.62607004 \times 10^{-34}\ \text{m}^2\,\text{kg}\,\text{s}^{-1}$ is the Planck constant, $c_0 = 299792485\ \text{m}\,\text{s}^{-1}$ is the speed of light in free space, and λ_0 is the free-space wavelength. The imaginary part of the refractive index is

$$\text{Im}\{n\} = \alpha_{\text{opt}}\frac{\lambda_0}{4\pi}. \tag{8}$$

The absorption coefficient α_{opt} is modeled in Ref. 29

$$\alpha_{\text{opt}}(\xi) = 10^5\sqrt{C(\xi)(E_\gamma - E_g) + D(\xi)(E_\gamma - E_g)^2}\ \text{nm}^{-1}, \tag{9}$$

where the constants

$$\left.\begin{aligned} C(\xi) &= (3.525 - 18.28\xi + 40.22\xi^2 - 37.52\xi^3 + 12.77\xi^4)\ \text{eV}^{-1} \\ D(\xi) &= (-0.6651 + 3.616\xi - 2.460\xi^2)\ \text{eV}^{-2} \end{aligned}\right\}, \tag{10}$$

come from interpolation of parameters given by Brown et al.[47]

An empirical low-field mobility model—called either the Caughey–Thomas [29] or the Arora [48] mobility model—describes the variations of the electron mobility μ_n and the hole mobility μ_p with temperature and doping. Thus

$$\mu_\ell = \mu_\ell^{(1)}\left(\frac{T}{T_{\text{ref}}}\right)^{\alpha_{ct,\ell}} + \frac{\mu_\ell^{(2)}\left(\frac{T}{T_{\text{ref}}}\right)^{\beta_\ell} - \mu_\ell^{(1)}\left(\frac{T}{T_{\text{ref}}}\right)^{\alpha_{ct,\ell}}}{1 + \left[\left(\frac{T}{T_{\text{ref}}}\right)^{-\gamma_\ell}\left(\frac{N_d+N_a}{N_\ell^{\text{crit}}}\right)\right]^{\delta_\ell}}, \qquad \ell \in \{n, p\}, \tag{11}$$

where $\ell = n$ for electrons and $\ell = p$ for holes. In the foregoing equation, $\mu_\ell^{(2)}$ is the maximum value of the carrier mobility μ_ℓ when the material is undoped, $\mu_\ell^{(1)}$ is the minimum value of μ_ℓ when the material is heavily doped, N_ℓ^{crit} is the critical doping density of the $\text{In}_\xi\text{Ga}_{1-\xi}\text{N}$ alloy, T is the lattice temperature and $T_{\text{ref}} = 300$ K is the reference temperature, and $\alpha_{ct,\ell}$, β_ℓ, γ_ℓ, and δ_ℓ are empirically determined parameters. The solar cell was taken to be operating at $T = T_{\text{ref}} = 300$ K; therefore, it should be noted that the choices of $\alpha_{ct,\ell}$, β_ℓ, and γ_ℓ have no effect on the results. Following Hamady et al.,[29] in lieu of experimental data, we assumed that $\alpha_{ct,\ell} = \beta_\ell = \gamma_\ell = 1$ for all simulations reported here. With these assumptions, the carrier mobilities simplify to

$$\mu_\ell = \mu_\ell^{(1)} + \frac{\mu_\ell^{(2)} - \mu_\ell^{(1)}}{1 + \tilde{N}_\ell^{\delta_\ell}}, \qquad \ell \in \{n, p\}, \tag{12}$$

where $\tilde{N}_\ell = (N_d + N_a)/N_\ell^{\text{ref}}$ is the ratio of doping density to the critical doping density. The electronic data used for $\text{In}_\xi\text{Ga}_{1-\xi}\text{N}$ presented in Table 1 were provided by Hamady et al.,[29] who

also demonstrated that a relatively large metal work-function Φ for the Schottky-barrier contact improves efficiency. Accordingly, the relatively large value of $\Phi = 6$ eV was chosen here.

The bandgap profile of $In_\xi Ga_{1-\xi}N$ for the solar cells simulated in this study is given by

$$E_{g0}(z) = E_g^* - A\left(1 - \left\{\frac{1}{2}\left[\sin\left(\frac{2\pi z}{L_p} - 2\pi\phi\right) + 1\right]\right\}^{\alpha}\right), \tag{13}$$

where E_g^* is the baseline (maximum) bandgap, A is the amplitude, $L_p = L_z/\kappa$ is the period with $\kappa > 0$, ϕ is a phase shift, and α is a shaping parameter, which governs the profile's gradient. Three example bandgap profiles are shown in Fig. 2 for $\alpha \in \{0.2, 1, 10\}$, when $\kappa = 3$ and $\phi = 0.75$.

2.2 *Computational Model*

A 2-D finite-element optoelectronic model was implemented in the COMSOL Multiphysics (V5.1) software package[48] in two major steps, as described now. Let it be noted that terms in block capitals are COMSOL Multiphysics[48] terms.

In the first major step, the ELECTROMAGNETIC WAVES, FREQUENCY DOMAIN module was used to calculate the 2-D EHP generation rate as a function of $x \in (-L_x/2, L_x/2]$ and $z \in (0, L_z)$. Normally incident monochromatic light sampled at 5-nm intervals on the λ_0-scale across the AM1.5G spectrum, 50% s polarized and 50% p polarized, was activated by the PERIODIC PORTS option at $z = -L_c - L_w - L_{\text{Air}}$. DIFFRACTION ORDER ports for diffraction orders $\{-3, -2, -1, 1, 2, 3\}$ were added. The inclusion of diffraction ports for even higher orders has little impact on the resulting EHP generation rate, predominantly due to strong absorption of shorter wavelength photons by $In_\xi Ga_{1-\xi}N$, the majority of which are absorbed close to the surface of the device before they can be scattered. The boundaries parallel to the z-axis have FLOQUET PERIODICITY with the wavevector provided by the periodic ports. The region $z > L_z + L + f$ behind the back reflector was taken to be a PERFECTLY MATCHED LAYER. The semiconductor region was first meshed with a MAPPED mesh with a 10-nm DISTRIBUTION in both the z- and x-directions and then split into to a triangular distribution using the insert center points conversion. The back-reflector region was covered with an EXTRA FINE, DELAUNAY, and FREE TRIANGULAR mesh. Data for a spatial map of the computed EHP generation rate were stored in an external file.

The EHP generation rate can be used to compute the optical short-circuit current density $J_{\text{SC}}^{\text{Opt}}$, assuming that every absorbed photon creates an EHP in the $In_\xi Ga_{1-\xi}N$ layer and that no recombination takes place. Neglect of recombination implies that $J_{\text{SC}}^{\text{Opt}}$ is necessarily larger than the short-circuit current density J_{SC}, which is the electronically simulated current density that flows when the solar cell is illuminated and no external bias is applied (i.e., when $V_{\text{ext}} = 0$).

In the second major step, the SEMICONDUCTOR module was used to calculate the electron and hole densities in the semiconductor region, and thereby the current densities. Due to the symmetry of the unit cell, only its right half (i.e., $0 \le x \le L_x/2$) needs to be electrically simulated.

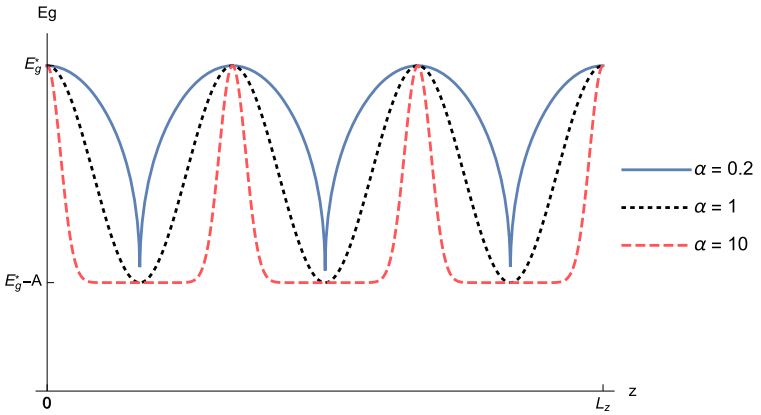

Fig. 2 Bandgap profiles given by Eq. (13) for $\alpha \in \{0.2, 1, 10\}$, when $\kappa = 3$ and $\phi = 0.75$.

FERMI-DIRAC CARRIER STATISTICS, along with CONTINUOUS QUASI-FERMI LEVELS at any internal boundary, were employed. FINITE VOLUME (CONSTANT SHAPE FUNCTION) discretization was employed as this inherently conserves current throughout the solar cell.[48] COMSOL uses a Scharfetter–Gummel upwinding scheme for solving the charge carrier transport equations. THE FREE TRIANGULAR, DELAUNAY mesh has a maximum element size of 15 nm.

A potential difference of V_{ext} was applied between the ohmic and IDEAL SCHOTTKY contacts. THERMIONIC CURRENTS, with standard Richardson coefficients of $A_n^* = 110\ \text{A K}^{-2}\,\text{cm}^{-2}$, and $A_p^* = 90\ \text{A K}^{-2}\,\text{cm}^{-2}$ were applied at the Schottky barrier.[29,48] INSULATOR INTERFACES were placed at the remaining external electrical boundaries. External Mathematica™ or MATLAB™ codes were used to calculate the USER-DEFINED GENERATION from the output of the first major step. Recombination was incorporated via AUGER, DIRECT and TRAP-ASSISTED (MIDGAP SHOCKLEY-READ-HALL) pathways, with parameters as provided in Table 1. To facilitate convergence, the nonhomogeneity, EHP generation, and EHP recombination physics were slowly activated as the solver progressed by use of a CONTINUATION PARAMETER. AN ANALYTIC DOPING MODEL was used to set the donor concentration to N_d. THE FREE TRIANGULAR, DELAUNAY mesh used has a maximum element size of 15 nm.

3 Numerical Simulations of $\text{In}_\xi\text{Ga}_{1-\xi}\text{N}$ Schottky-Barrier Solar Cells

3.1 *Design of Periodically Corrugated Back Reflector*

The numerical results presented here are for devices with parameters listed in Table 2. A preliminary study was carried out to ascertain reasonable values for the dimensions of the device. Figure 3 presents $J_{\text{SC}}^{\text{Opt}}$ as a function of the back-reflector period $L_x \in (300,1000)\,\text{nm}$ for a Schottky-barrier solar cell with a homogeneous $\text{In}_\xi\text{Ga}_{1-\xi}\text{N}$ layer of thickness

Table 2 Summary of parameters used for the simulations.

	Symbol	Value
Device width	L_x	600 nm
n-doped $\text{In}_\xi\text{Ga}_{1-\xi}\text{N}$ thickness	L_z	600 nm
Back reflector insulating layer thickness	d_a	135 nm
Corrugation height	L_g	130 nm
Corrugation duty cycle	ζ	0.5
Metal thickness	L_m	100 nm
Contact region thickness	L_c	5 nm
Ohmic contact width	L_o	140 nm
Schottky contact width	L_s	440 nm
AR window thickness	L_w	100 nm
Air thickness	L_{Air}	500 nm
Predoping bandgap	E_{g0}	[0.7,3.42] eV
Bandgap-nonhomogeneity amplitude	A	≥0 eV
Bandgap-nonhomogeneity phase	ϕ	[0,1]
Bandgap-nonhomogeneity shaping parameter	α	(0,32)
Bandgap-nonhomogeneity period	L_p	>0 nm
Bandgap-nonhomogeneity ratio	κ	>0

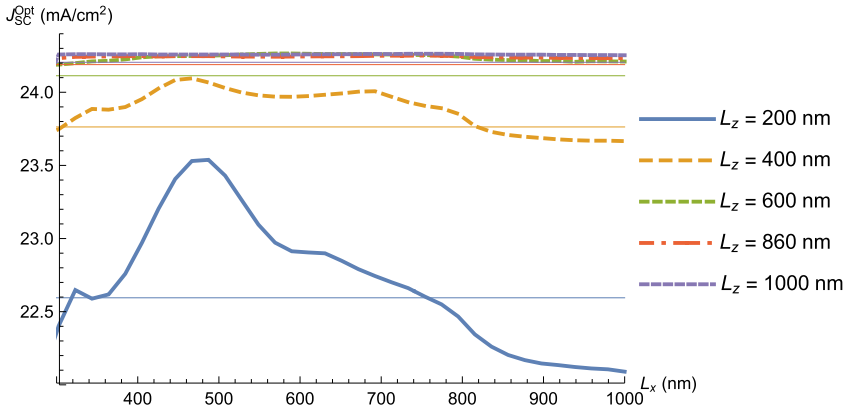

Fig. 3 Optical short-circuit current density J_{SC}^{Opt} as a function of the back-reflector period L_x for a Schottky-barrier solar cell with $In_\xi Ga_{1-\xi}N$ layer of thickness $L_z \in \{200,400,600,860,1000\}$ nm. The absorbing layer of $In_\xi Ga_{1-\xi}N$ is homogeneous with $\xi = 0.6$, i.e., the bandgap $E_{g0} = 1.45$ eV. Thin solid lines show J_{SC}^{Opt} for the equivalent solar cells with a flat back-reflector.

$L_z \in \{200,400,600,860,1000\}$ nm. For this set of simulations, $L_g = 130$ nm, $d_a = 135$ nm, and $\zeta = 0.5$ were determined as optimal for a solar cell with a homogeneous $In_\xi Ga_{1-\xi}N$ layer characterized by $E_{g0} = 1.6$ eV, $L_x = 600$ nm, and $L_z = 860$ nm. While this optimization is far from exhaustive, significant optical variation was seen to occur for thinner $In_\xi Ga_{1-\xi}N$ solar cells: a 6% variation in J_{SC}^{Opt} was calculated for a solar cell with $L_z = 200$ nm, with a maximum J_{SC}^{Opt} of 24.9 mA cm^{-2} when $L_x = 480$ nm. Importantly, for solar cells with $In_\xi Ga_{1-\xi}N$ layers thicker than about 600 nm, J_{SC}^{Opt} saturates as L_x increases beyond a threshold value. Therefore, $L_x = 600$ nm was chosen to be optimal. While the peak value of J_{SC} of a Schottky-barrier solar cell with a 600-nm-thick $In_\xi Ga_{1-\xi}N$ layer is obtained for larger periods than this ($L_x \approx 680$ nm), J_{SC} falls more rapidly for devices with back reflectors of overly large periods than for those with periods that are too small.

3.2 *Effect of Periodic Nonhomogeneity of $In_\xi Ga_{1-\xi}N$ Layer*

The essential effects of including periodic nonhomogeneity in the thickness direction in the $In_\xi Ga_{1-\xi}N$ layer may be inferred from Fig. 4. For a fixed bandgap-nonhomogeneity amplitude $A \in \{0, 0.2, 0.4, 0.6, 0.8, 1\}$, the baseline bandgap E_g^* is shown to dramatically affect the simulated efficiency

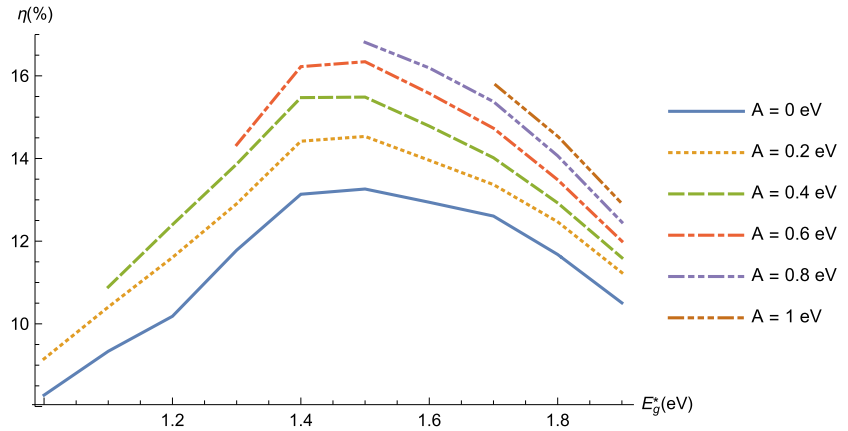

Fig. 4 Efficiency η as a function of baseline bandgap E_g^* for bandgap-nonhomogeneity amplitude $A \in \{0, 0.2, 0.4, 0.6, 0.8, 1\}$ eV, when $\kappa = 3$, $\alpha = 2$, and $\phi = 0.75$.

$$\eta = \max_{V_{\text{ext}}} \frac{V_{\text{ext}} J(V_{\text{ext}})}{1000\ \text{W/m}^2}, \tag{14}$$

which equals the maximum power produced by the solar cell as a function of V_{ext}, divided by the incident AM1.5G solar power flux of 1000 W/m^2. The solar spectrum was discretized at 5-nm λ_0-intervals; with the minimum λ_0 chosen to be 300 nm; the maximum λ_0 chosen as $\min[2400, 1240/(E_g^* - A)]$ nm; the other bandgap-nonhomogeneity parameters fixed at $\kappa = 3$, $\alpha = 2$, and $\phi = 0.75$. At the minimum bandgap for an $In_\xi Ga_{1-\xi}N$ alloy, i.e., $E_g = 0.7$ V which arises at $\xi = 1$, there is a minimum permissible baseline bandgap E_g^* for each value of A. Irrespective of the choice of value of $A \in (0, 0.8)$ eV, a baseline bandgap of $E_g^* = 1.5$ eV turns out to be optimal. From Fig. 4, it may be inferred that the difference in the efficiencies with a homogeneous $In_\xi Ga_{1-\xi}N$ layer and a periodically nonhomogeneous $In_\xi Ga_{1-\xi}N$ layer is greatest when

a. the bandgap-nonhomogeneity amplitude A is the greatest and
b. when the maximum bandgap $E_g^* \approx 1.5$ eV.

Indeed, at $E_g^* = 1.5$ eV, the efficiency is 13.26% for $A = 0$ and 16.81% for $A = 0.8$ eV, i.e., the relative increase in efficiency attributable to the periodic nonhomogeneity of the $In_\xi Ga_{1-\xi}N$ layer is 26.8%, which is this paper's most significant result. For $A = 1$ eV, $E_g^* = 1.7$ eV is optimal, yielding an efficiency of 15.8%.

The importance of the periodicity in the bandgap variation when seeking maximal efficiency may be inferred from Figs. 5 and 6. In Fig. 5, the thickness of the $In_\xi Ga_{1-\xi}N$ layer is fixed at $L_z = 600$ nm while the ratio κ varies from 0.5 to 4. The efficiency of the solar cell is seen to reach a maximum value of about 17% at $\kappa = 1.4$ and $\kappa = 3$. Between these two values of κ, only a slight decrease in η was found. Significantly, the efficiency for all values of $\kappa > 0$ is greater than it is when the $In_\xi Ga_{1-\xi}N$ layer is homogeneous.

Figure 6 illustrates the effect of varying the thickness L_z of the $In_\xi Ga_{1-\xi}N$ layer when the nonhomogeneity period L_p is fixed. Irrespective of the period, the solar cell with the nonhomogeneous $In_\xi Ga_{1-\xi}N$ layer performs better than the one with a homogeneous $In_\xi Ga_{1-\xi}N$ layer. Furthermore, the solar cell with the smaller period ($L_p = 200$ nm) is found to perform more efficiently than the one with larger period ($L_p = 400$ nm). Distinct maximums can be seen at $\kappa = 1.5$ and $\kappa = 3$, which correspond to $L_z = 300$ nm and $L_z = 600$ nm, respectively. The efficiencies at these points, respectively, are 17.28% and 16.88%, which correspond to relative increases in efficiency of 16.7% and 28.5% as compared to the analogous solar cell with a homogeneous $In_\xi Ga_{1-\xi}N$ layer.

By varying the bandgap-nonhomogeneity shaping parameter α, the spatial profile of the $In_\xi Ga_{1-\xi}N$ nonhomogeneity can be varied. Thus, $\alpha = 1$ holds for a sinusoidal bandgap profile,

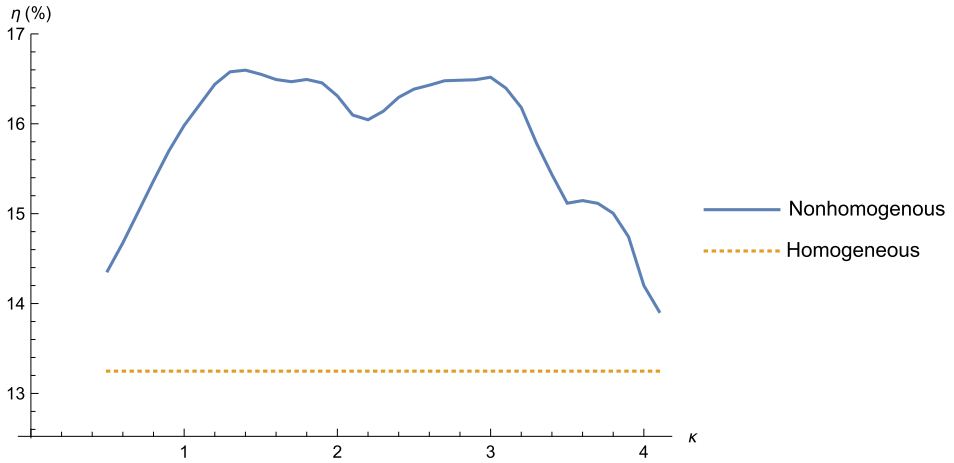

Fig. 5 Efficiency η as a function of the ratio $\kappa = L_z/L_p$ for the $In_\xi Ga_{1-\xi}N$ layer when $L_z = 600$ nm, $E_g^* = 1.5$ eV, $A = 0.8$ eV, $\alpha = 2$, and $\phi = 0.75$. The horizontal red line indicates the efficiency when the $In_\xi Ga_{1-\xi}N$ layer is homogeneous.

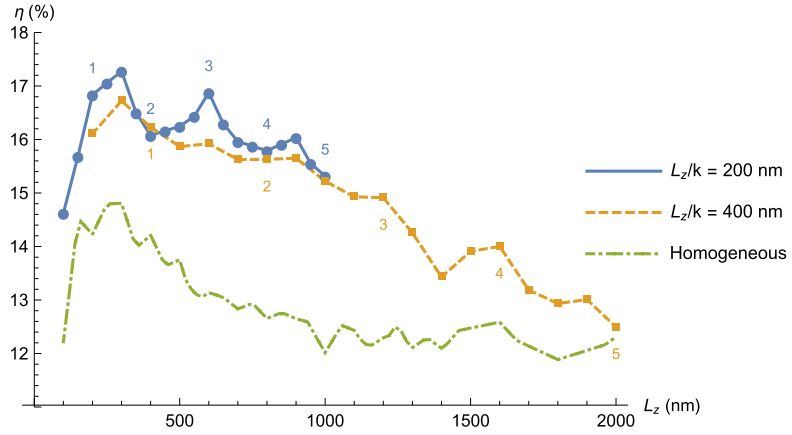

Fig. 6 Efficiency η as a function of thickness L_z of the $In_\xi Ga_{1-\xi}N$ layer, which is either homogeneous (solid black curve) or periodically nonhomogeneous with $L_p = 200$ nm (dashed red curve) or $L_p = 400$ nm (dotted blue curve), when $E_g^* = 1.54$ eV, $A = 0.8$ eV, $\alpha = 5$, and $\phi = 0.75$. Integer values of the ratio $\kappa = L_z/L_p$ are identified.

while smaller and larger values of α yield bandgap profiles with steeper gradients, as illustrated in Fig. 2. For all three values of α in Fig. 7, the efficiency of the solar cell is substantially greater than it is for the corresponding solar cell with a homogeneous $In_\xi Ga_{1-\xi}N$ layer. The maximum increase in efficiency is found for a nearly sinusoidal bandgap profile; indeed, the efficiency increases from 13.2% for a Schottky-barrier solar cell with a homogeneous $In_\xi Ga_{1-\xi}N$ layer to 16.88% for its analog with a nonhomogeneous $In_\xi Ga_{1-\xi}N$ layer with $\alpha = 2$, which is a relative increase in efficiency of 28.5%.

Let us note here that as α becomes much larger or smaller than unity, the spatial gradients of the bandgap increase in magnitude and the peaks in Fig. 2 become narrower. Accordingly, at extreme values of α, the semiclassical carrier-transport equations implemented in our model become less appropriate as quantum processes become significant. Then, it may be necessary to take into account the quantization of allowed energy states between the peaks of $E_{g0}(z)$ and tunneling through those peaks, especially for large amplitudes A.

4 Closing Remarks

A 2-D finite-element model was devised to simulate the combined optical and electrical performances of $In_\xi Ga_{1-\xi}N$ Schottky-barrier solar cells. First, it was found that a periodically

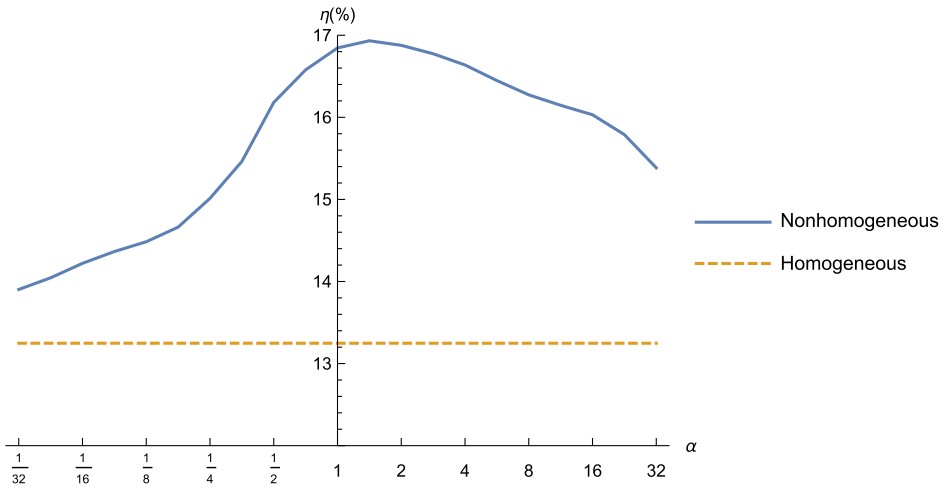

Fig. 7 Efficiency η plotted against bandgap-nonhomogeneity shaping parameter α, when $E_g^* = 1.54$ eV, $A = 0.8$ eV, $L_z = 600$ nm, $\kappa = 3$, and $\phi = 0.75$.

corrugated back reflector of a period of 600 nm is optimal for photon absorption in a solar cell containing a homogeneous layer of $In_{\xi}Ga_{1-\xi}N$. Second, the effects of periodic nonhomogeneity of the $In_{\xi}Ga_{1-\xi}N$ layer were elucidated. The nonhomogeneity was directed perpendicular to the mean plane of the periodically corrugated back reflector. For the particular model investigated here, the efficiency of a solar cell with a 600-nm-thick layer of $In_{\xi}Ga_{1-\xi}N$ was found to increase by 26.8% when suitable periodic nonhomogeneity was incorporated. Thus, the incorporation of a periodically nonhomogeneous $In_{\xi}Ga_{1-\xi}N$ layer in a Schottky-barrier solar cell can substantially increase the efficiency as compared to the analogous solar cell with a homogeneous $In_{\xi}Ga_{1-\xi}N$ layer. A comprehensive optimization of study of material and design parameters may well yield even greater nonhomogeneity-induced increases in efficiency. However, such an optimization study—which is justified by the substantial efficiency boosts reported herein—represents a major undertaking that lies beyond the scope of this paper. Similarly, it would be of some value to delineate the photon-absorption mechanisms that underpin the boost in the light-to-electricity conversion efficiency that arises following the introduction of periodic nonhomogeneity, but this too is matter for future study.

The feasibility of producing $In_{\xi}Ga_{1-\xi}N$ alloys with the prescribed spatial variation in ξ to achieve efficiency boosts in Schottky-barrier solar cells is a matter for our experimentalist colleagues to shed light on. On the basis of our numerical study and the relatively huge boosts in efficiency that may be attained, it would be worthwhile for major efforts to be directed toward the production of appropriate $In_{\xi}Ga_{1-\xi}N$ alloys.

Last, the principal finding of our study is that the introduction of periodic nonhomogeneity can, in principle, substantially boost the efficiency of a Schottky-barrier solar cell. To focus on efficiency, our attention was restricted to only normally incident solar radiation for all cell configurations considered. The influence of the angle of incidence is planned for a future study in which the mechanisms for efficiency boosting will be more fully explored.

Acknowledgments

T.H.A. thanks the Charles Godfrey Binder Endowment for partial financial support during a six-month stay at Pennsylvania State University. T.G.M. acknowledges the support of EPSRC Grant No. EP/M018075/1. A.L. thanks the National Science Foundation for partial financial support under Grant No. DMS-1619901, and he is grateful to the Charles Godfrey Binder Endowment for ongoing support of his research.

References

1. R. Singh, G. F. Alapatt, and A. Lakhtakia, "Making solar cells a reality in every home: opportunities and challenges for photovoltaic device design," *IEEE J. Electron Devices Soc.* **1**, 129–144 (2013).
2. P. Verlinden et al., "The surface texturization of solar cells: a new method with V-grooves with controllable sidewall angles," *Sol. Energy Mater. Sol. Cells* **26**, 71–78 (1992).
3. N. Yamada et al., "Characterization of antireflection moth-eye film on crystalline silicon photovoltaic module," *Opt. Express* **19**, A118–A125 (2011).
4. P. Sheng, A. N. Bloch, and R. S. Stepleman, "Wavelength-selective absorption enhancement in thin-film solar cells," *Appl. Phys. Lett.* **43**, 579–581 (1983).
5. C. Heine and R. F. Morf, "Submicrometer gratings for solar energy applications," *Appl. Opt.* **34**, 2476–2482 (1995).
6. M. Solano et al., "Optimization of the absorption efficiency of an amorphous-silicon thin-film tandem solar cell backed by a metallic surface-relief grating," *Appl. Opt.* **52**, 966–979 (2013) [errata: 54398–399 (2015)].
7. S. K. Dhungel et al., "Double-layer antireflection coating of MgF_2/SiN_x for crystalline silicon solar cells," *J. Korean Phys. Soc.* **49**, 885–889 (2006).
8. S. A. Boden and D. M. Bagnall, "Sunrise to sunset optimization of thin film antireflective coatings for encapsulated, planar silicon solar cells," *Prog. Photovoltaics Res. Appl.* **17**, 241–252 (2009).

9. D. M. Schaadt, B. Feng, and E. T. Yu, "Enhanced semiconductor optical absorption via surface plasmon excitation in metal nanoparticles," *Appl. Phys. Lett.* **86**, 063106 (2005).
10. J.-Y. Lee and P. Peumans, "The origin of enhanced optical absorption in solar cells with metal nanoparticles embedded in the active layer," *Opt. Express* **18**, 10078–10087 (2010).
11. P. Shokeen, A. Jain, and A. Kapoor, "Silicon nanospheres for directional scattering in thin-film solar cells," *J. Nanophotonics* **10**, 036013 (2016).
12. R. A. Sinton et al., "27.5-percent silicon concentrator solar cells," *IEEE Electron Device Lett.* **7**, 567–569 (1986).
13. K. Nishioka et al., "Evaluation of InGaP/InGaAs/Ge triple-junction solar cell and optimization of solar cells structure focusing on series resistance for high-efficiency concentrator photovoltaic systems," *Sol. Energy Mater. Sol. Cells* **90**, 1308–1321 (2006).
14. M. E. Solano et al., "Buffer layer between a planar optical concentrator and a solar cell," *AIP Adv.* **5**, 097150 (2015).
15. L. Liu et al., "Planar light concentration in micro-Si solar cells enabled by a metallic grating-photonic crystal architecture," *ACS Photonics* **3**, 604–610 (2016).
16. T. H. Anderson et al., "Combined optical-electrical finite-element simulations of thin-film solar cells with homogeneous and nonhomogeneous intrinsic layers," *J. Photonics Energy* **6**, 025502 (2016).
17. L. Liu et al., "Experimental excitation of multiple surface-plasmon-polariton waves and waveguide modes in a one-dimensional photonic crystal atop a two-dimensional metal grating," *J. Nanophotonics* **9**, 093593 (2015).
18. L. M. Anderson, "Parallel-processing with surface plasmons, a new strategy for converting the broad solar spectrum," in *Proc. 16th IEEE Photovoltaic Specialists Conf.*, Vol. **1**, pp. 371–377 (1982).
19. L. M. Anderson, "Harnessing surface plasmons for solar energy conversion," *Proc. SPIE* **408**, 172–178 (1983).
20. J. A. Polo, Jr., T. G. Mackay, and A. Lakhtakia, *Electromagnetic Surface Waves: A Modern Perspective*, Elsevier, Waltham, Massachusetts (2013).
21. T. Khaleque and R. Magnusson, "Light management through guided-mode resonances in thin-film silicon solar cells," *J. Nanophotonics* **8**, 083995 (2014).
22. M. Faryad and A. Lakhtakia, "Enhancement of light absorption efficiency of amorphous-silicon thin-film tandem solar cell due to multiple surface-plasmon-polariton waves in the near-infrared spectral regime," *Opt. Eng.* **52**, 087106 (2013) [errata: 53129801 (2014)].
23. M. I. Kabir et al., "Amorphous silicon single-junction thin-film solar cell exceeding 10% efficiency by design optimization," *Int. J. Photoenergy* **2012**, 460919 (2012).
24. S. M. Iftiquar et al., "Single- and multiple-junction p-i-n type amorphous silicon solar cells with $p-a-Si_{1-x}C_x:H$ and nc-Si:H films," in I. Yun, Ed., *Photodiodes—From Fundamentals to Applications*, InTech, Rijeka, Croatia (2012).
25. P. T. Landsberg and C. Klimpke, "Theory of the Schottky barrier solar cell," *Proc. R. Soc. A: Math. Phys. Eng. Sci.* **354**, 101–118 (1977).
26. N. K. Swami, S. Srivastava, and H. M. Ghule, "The role of the interfacial layer in Schottky barrier solar cells," *J. Phys. D: Appl. Phys.* **12**, 765–771 (1979).
27. J.-P. Colinge and C. A. Colinge, *Physics of Semiconductor Devices*, Kluwer Academic, New York, New York (2002).
28. P. Mahala et al., "Metal/InGaN Schottky junction solar cells: an analytical approach," *Appl. Phys. A* **118**, 1459–1468 (2015).
29. S. O. S. Hamady, A. Adaine, and N. Fressengeas, "Numerical simulation of InGaN Schottky solar cell," *Mater. Sci. Semicond. Process.* **41**, 219–225 (2016).
30. J.-J. Xue et al., "Au/Pt/InGaN/GaN heterostructure Schottky prototype solar cell," *Chin. Phys. Lett.* **26**, 098102 (2009).
31. J. Wu et al., "Superior radiation resistance of $In_xGa_{1-x}N$ alloys: full-solar-spectrum photovoltaic material system," *J. Appl. Phys.* **94**, 6477–6482 (2003).
32. J. Wu et al., "Unusual properties of the fundamental band gap of InN," *Appl. Phys. Lett.* **80**, 3967–3969 (2002).
33. Y. Saito et al., "Growth temperature dependence of Indium Nitride crystalline quality grown by RF-MBE," *Physica Status Solidi B* **234**, 796–800 (2002).

34. S. X. Li et al., "Fermi-level stabilization energy in group III nitrides," *Phys. Rev. B* **71**, 161201 (2005).
35. K. Osamura et al., "Fundamental absorption edge in GaN, InN and their alloys," *Solid State Commun.* **11**, 617–621 (1972).
36. T. Yodo et al., "Strong band edge luminescence from InN films grown on Si substrates by electron cyclotron resonance-assisted molecular beam epitaxy," *Appl. Phys. Lett.* **806**, 968–970 (2002).
37. T. H. Anderson et al., "Towards numerical simulation of nonhomogeneous thin-film silicon solar cells," *Proc. SPIE* **8981**, 898115 (2014).
38. X. Y. Gao, Y. Liang, and Q. G. Lin, "Analysis of the optical constants of aluminum-doped zinc-oxide films by using the single-oscillator model," *J. Korean Phys. Soc.* **57**, 710–714 (2010).
39. E. D. Palik, Ed., *Handbook of Optical Constants of Solids*, Academic Press, Boston, Massachusetts (1985).
40. "Reference solar spectral irradiance: air mass 1.5," NREL, http://rredc.nrel.gov/solar/spectra/am1.5/ (28 July, 2015).
41. J. Nelson, *The Physics of Solar Cells*, Imperial College Press, London, United Kingdom (2003).
42. S. J. Fonash, *Solar Cell Device Physics*, 2nd ed., Academic Press, Burlington, Massachusetts (2010).
43. J. Wu and W. Walukiewicz, "Band gaps of InN and group III nitride alloys," *Superlattices Microstruct.* **34**, 63–75 (2003).
44. L. Vegard, "Die Röntgenstrahlen im Dienste der Erforschung der Materie," *Z. Kristallogr.* **67**, 239–259 (1928).
45. J. W. Slotboom and H. C. de Graaff, "Measurements of bandgap narrowing in Si bipolar transistors," *Solid-State Electron.* **19**, 857–862 (1976).
46. I.-H. Lee et al., "Band-gap narrowing and potential fluctuation in Si-doped GaN," *Appl. Phys. Lett.* **74**, 102–104 (1999).
47. G.F. Brown et al., "Finite element simulations of compositionally graded InGaN solar cells," *Sol. Energy Mater. Sol. Cells* **94**, 478–483 (2010).
48. http://www.comsol.com/ (19 January 2015).

Tom H. Anderson received his BSc degree in mathematics and physics from the University of Edinburgh in 2011. He received his MSc degree in fusion energy from the University of York in 2012 and his PhD in applied mathematics from the University of Edinburgh in 2016. His research interests include the optical and electrical modeling of thin-film solar cells.

Tom G. Mackay is a reader at the School of Mathematics, the University of Edinburgh, and an adjunct professor in the Department of Engineering Science and Mechanics at Pennsylvania State University. He is a graduate of the Universities of Edinburgh, Glasgow, and Strathclyde and a fellow of the Institute of Physics (UK) and SPIE. His research interests include the electromagnetic theory of complex materials, including homogenized composite materials.

Akhlesh Lakhtakia received degrees from the Banaras Hindu University and the University of Utah. He is the Charles Godfrey Binder professor of engineering at the Pennsylvania State University. His research interests include surface multiplasmonics, bioreplication, forensic science, solar cells, sculptured thin films, and mimumes. He is a fellow of Optical Society of America, SPIE, Institute of Physics, American Association for the Advancement of Science, American Physical Society, Institute of Electrical and Electronics Engineers, and Royal Society of Chemistry. He received the 2010 SPIE Technical Achievement Award and the 2016 Walston Chubb Award for Innovation.